A general electrolyte–electrode-assembly model for the performance characteristics of planar anode-supported solid oxide fuel cells

M.M. Hussain[a], X. Li[a,*], I. Dincer[b]

[a] Department of Mechanical and Mechatronics Engineering, University of Waterloo, Waterloo, Ontario, Canada N2L 3G1
[b] Faculty of Engineering and Applied Science, University of Ontario Institute of Technology Oshawa, Ontario, Canada L1H 7K4

ARTICLE INFO

ABSTRACT

A general electrode–electrolyte-assembly (EEA) model has been developed, which is valid for different designs of solid oxide fuel cells (SOFCs) operating at different temperatures. In this study, it is applied to analyze the performance characteristics of planar anode-supported SOFCs. One of the novel features of the present model is its treatment of electrodes. An electrode in the present model is composed of two distinct layers referred to as the backing layer and the reaction zone layer. The other important feature of the present model is its flexibility in fuel, having taking into account the reforming and water–gas shift reactions in the anode. The coupled governing equations of species, charge and energy along with the constitutive equations in different layers of the cell are solved using finite volume method. The model can predict all forms of overpotentials and the predicted concentration overpotential is validated with measured data available in literature. It is found that in an anode-supported SOFC, the cathode overpotential is still the largest cell potential loss mechanism, followed by the anode overpotential at low current densities; however, the anode overpotential becomes dominant at high current densities. The cathode and electrolyte overpotentials are not negligible even though their thicknesses are negligible relative to the anode thickness. Even at low fuel utilizations, the anode concentration overpotential becomes significant when chemical reactions (reforming and water–gas shift) in the anode are not considered. A parametric study has also been carried out to examine the effect of various key operating and design parameters on the performance of an anode-supported planar SOFCs.

© 2008 Elsevier B.V. All rights reserved.

1. Introduction

Solid oxide fuel cells (SOFCs) are receiving considerable attention for stationary power applications due to their high energy efficiency, low pollutant emissions, fuel flexibility, and co-generation capability. Among various configurations in which SOFCs exist, two common configurations are tubular and planar. Although significant progresses have been made for the tubular configuration of SOFC, tubular SOFC has low power density due to high electrical resistance arising from long current paths [1]. In contrast, the planar configuration of SOFC is capable of achieving very high power density [1,2]. However, due to high temperature operation, there exist technical challenges for planar SOFCs, such as requirement of high temperature gas seals, high material and manufacturing costs. Therefore, it is important to reduce the operating temperature to an intermediate range (823–1073 K), often referred to as intermediate-temperature SOFCs; then, conventional stainless steel can be used for interconnects instead of more expensive high

chrome alloys or oxides, and the material and manufacturing costs can be reduced significantly [3,4].

Planar SOFCs are generally fabricated into two basic designs, namely electrolyte-supported and electrode-supported. In electrolyte-supported SOFCs, electrolyte is the thickest component on which anode and cathode layers are deposited. Since electrolyte is the thickest component, the ohmic contribution of the electrolyte layer is significant in electrolyte-supported SOFCs; therefore, they are applicable for high temperature operation with the typical electrolyte material, which is yttria stabilized zirconia (YSZ) [5]. On the other hand, in electrode-supported SOFCs, either anode or cathode is the thickest component on which all other layers are deposited. Among electrode-supported SOFCs, anode-supported design is preferred over cathode-supported design for operation at reduced temperatures. This is due to higher contribution of cathode overpotentials to the total cell potential loss than the anode, especially at reduced operating temperatures [5,6].

The processes influencing an SOFC performance in different layers of the cell are complex, competing and interdependent. Because of expensive and time consuming physical prototyping, experimental advances are quite limited. Hence, to enhance the development

---

Nomenclature

A_v	reactive surface area per unit volume ($m^2\,m^{-3}$)
c_{H_2}	hydrogen concentration ($mole\,m^{-3}$)
$c_{H_2,ref}$	reference hydrogen concentration ($mole\,m^3$)
c_{O_2}	oxygen concentration ($mole\,m^{-3}$)
$c_{O_2,ref}$	reference oxygen concentration ($mole\,m^{-3}$)
c_{pi}	specific heat of species i at constant pressure ($J\,mole^{-1}\,K^{-1}$)
d_p	diameter of the pore (μm)
D_{ij}	binary diffusion coefficient ($m^2\,s^{-1}$)
$D_{Kn,i}$	Knudsen diffusion coefficient ($m^2\,s^{-1}$)
$\mathcal{D}_{ij}^{eff}$	effective diffusion coefficient ($m^2\,s^{-1}$)
F	Faraday's constant ($96{,}487\,C\,mole^{-1}$)
h_i	absolute enthalpy of species i ($J\,mole^{-1}$)
J	current density ($A\,m^{-2}$)
J_e	electronic current density ($A\,m^{-2}$)
J_i	ionic current density ($A\,m^{-2}$)
$J_{0,ref}^{H_2}$	reference exchange current density for H_2 oxidation ($A\,m^{-2}$)
$J_{0,ref}^{O_2}$	reference exchange current density for O_2 reduction ($A\,m^{-2}$)
k	thermal conductivity ($W\,m^{-1}\,K^{-1}$)
k_{el}	thermal conductivity of pure electron-conducting particles ($W\,m^{-1}\,K^{-1}$)
k_f	thermal conductivity of fluid mixture ($W\,m^{-1}\,K^{-1}$)
k_i	thermal conductivity of pure component i ($W\,m^{-1}\,K^{-1}$)
k_{io}	thermal conductivity of pure electron-conducting particles ($W\,m^{-1}\,K^{-1}$)
k_s	thermal conductivity of solid phase of backing layers ($W\,m^{-1}\,K^{-1}$)
k_{br}	backward reaction rate constant for reforming reaction ($mole\,m^{-3}\,Pa^{-2}\,s^{-1}$)
k_{fr}	forward reaction rate constant for reforming reaction ($mole\,m^{-3}\,Pa^{-2}\,s^{-1}$)
k_{bs}	backward reaction rate constant for shift reaction ($mole\,m^{-3}\,Pa^{-2}\,s^{-1}$)
k_{fs}	forward reaction rate constant for shift reaction ($mole\,m^{-3}\,Pa^{-2}\,s^{-1}$)
K_p	equilibrium constant for partial pressure
K_{pr}	equilibrium constant for reforming reaction
K_{ps}	equilibrium constant for shift reaction
M_i	molecular weight of species i ($kg\,mole^{-1}$)
n	moles of electrons transferred per mole reactant
n_{el}	number fraction of electron-conducting particles in the reaction zone layers
n_{io}	number fraction of ion-conducting particles in the reaction zone layers
n_t	total number of particles in the reaction zone layers per unit volume m^{-3}
N_i	molar flux of species i ($mole\,m^{-2}\,s^{-1}$)
p	pressure (Pa)
p_{el}	probability of percolation of electron-conducting particles in reaction zone layers
p_{io}	probability of percolation of ion-conducting particles in reaction zone layers
p_i	partial pressure of species i (Pa)
q	heat flux ($W\,m^{-2}$)
r_{el}	radius of electron-conducting particles in the reaction zone layers (m)
r_{io}	radius of ion-conducting particles in the reaction zone layers (m)

r_i	rate of reaction ($mole\,m^{-2}\,s^{-1}$)
r_r	volumetric reforming reaction rate ($kg\,m^{-3}\,s^{-1}$)
r_s	volumetric shift reaction rate ($kg\,m^{-3}\,s^{-1}$)
R	universal gas constant ($8.3143\,J\,mole^{-1}\,K^{-1}$)
$\mathcal{R}_a$	volumetric current density produced due to hydrogen oxidation ($A\,m^{-3}$)
$\mathcal{R}_c$	volumetric current density produced due to oxygen reduction ($A\,m^{-3}$)
$\Delta\bar{s}_{H_2}$	molar entropy change for an overall fuel cell reaction involving hydrogen ($J\,mole^{-1}\,K^{-1}$)
$\Delta\bar{s}^o$	molar entropy change for a reaction at standard pressure ($J\,mole^{-1}\,K^{-1}$)
$\dot{S}_e$	rate of production or consumption of energy ($W\,m^{-3}$)
$\dot{S}_{s,i}$	rate of production or consumption of species i ($mole\,m^{-3}\,s^{-1}$)
T	temperature (K)
x_i	mole fraction of species i
Z	average coordination number
Z_{el}	coordination number of electron-conducting particles in the reaction zone layers
Z_{io}	coordination number of ion-conducting particles in the reaction zone layers

Greek symbols

α	charge transfer coefficient
γ_{H_2}	reaction order for hydrogen oxidation reaction
ε	porosity
η	electrode activation overpotential (anode or cathode) (V)
θ	contact angle between electron- and ion-conducting particles in the reaction zone layers
κ	ionic conductivity ($S\,m^{-1}$)
μ_i	dynamic viscosity of pure component i ($kg\,m^{-1}\,s^{-1}$)
ν_{H_2}	stoichiometric coefficient of H_2 involved in the oxidation reaction
ν_{O_2}	stoichiometric coefficient of OH_2 involved in the reduction reaction
ξ	fraction of entropy change of the overall SOFC reaction
σ	electronic conductivity ($S\,m^{-1}$)
τ	tortuosity
ϕ_e	electronic potential (V)
ϕ_i	ionic potential (V)
Φ	volume fraction of electron-conducting particles in the reaction zone layers
Φ_{ij}	dimensionless function

Subscripts

bl	backing layer
el	electrolyte layer
ref	reference
rl	reaction zone layer

Superscripts

eff	effective

and understanding of SOFCs, it is imperative to develop a mathematical model which accounts for complex transport processes with chemical and electrochemical reactions. The present model can be used to predict cell performance and gain insights on the physical, chemical and electrochemical processes occurring in different layers of the cell.

Over the past few years, many researchers have developed anode-supported SOFC models [3,5,7–11], which can be broadly classified into macro- or micro-models, depending on the treatment of electrodes. In macro-models, electrodes are modeled as porous structures of purely electron-conducting particles and electrochemical reactions are considered to occur exclusively at the electrode/electrolyte interfaces, thereby treating reaction zone layers as interfacial boundary conditions [3,5,8–11]. Whereas, in micro-models, electrodes are modeled as porous structures of electron- and ion-conducting particles. Essentially, electrodes in micro-models are treated as reaction zone layers having triple phase boundaries (TPBs) scattered throughout the electrodes [7,12–15,41]. However, most of the micro-models are electrode-level models predicting the electrochemical characteristics of an electrode, either anode or cathode; only recently Nam and Jeon [7] integrated this approach into a cell-level model. Additionally, Nam and Jeon [7] and many others [12,15–18] concluded that the TPBs are most active at the electrode/electrolyte interface and most of the electrochemical reactions in the electrodes occur within a distance of the order of 10 μm from the electrolyte. Conversely, most of the macro-models are cell-level models predicting the cell performance at different operating and design conditions. Incorporation of micro-characteristics of electrodes into macro-models not only helps in better understanding the relevant processes occurring within the electrodes, but also enhances the predicting capability of the overall cell model. One of the novelties of the present model is its treatment of the electrodes. An electrode in the present model is treated as two distinct layers referred to as the backing layer and the reaction zone layer for electrochemical reactions, thus serving as a bridge connecting the micro- and macro-approach of modeling electrodes. The other important feature of the present model is its flexibility in fuel choice; not only pure H_2 but also any reformate composition (H_2, H_2O, CO, CO_2 and CH_4) can be used as a fuel. Further, the modified Stefan–Maxwell equations incorporating Knudsen diffusion are used to model multi-component diffusion in the porous electrodes. Moreover, chemical reactions such as water–gas shift reaction and methane reforming reaction are considered in the anode of an SOFC.

The objective of this study is to develop a mathematical model of an SOFC that combines the micro- and macro-models and takes into account all the relevant physical, chemical and electrochemical processes in different layers of the cell and predicts all forms of overpotentials. The developed model is then applied to analyze performance characteristics of planar anode-supported SOFCs. Finally, the effect of various key operating and design conditions on the performance of an anode-supported SOFC is investigated.

2. Model formulation

A schematic of a planar anode-supported SOFC is shown in Fig. 1. Since the geometry is symmetric about the middle-axis of the flow channel, the schematic shown is the right half cross-section of the cell. A typical anode-supported SOFC consists of a thick anode, a relatively thinner electrolyte and cathode. However, in the present formulation, two finite distinct layers are considered between the electrodes and the electrolyte, which are referred to as the anode reaction zone layer and the cathode reaction zone layer, respectively. The computational domain is shown by a dashed line, which includes the land portion of the interconnects interfacing the backing layers, the porous portion of the backing layers interfacing the flow channels, the backing layers, the reaction zone layers, and the electrolyte layer.

The cell is assumed to operate under steady state and the parameters vary in the x (across the cell) and y (transverse) directions. The convective flux is negligible in the porous backing and reaction zone layers when compared to the diffusive flux of gaseous
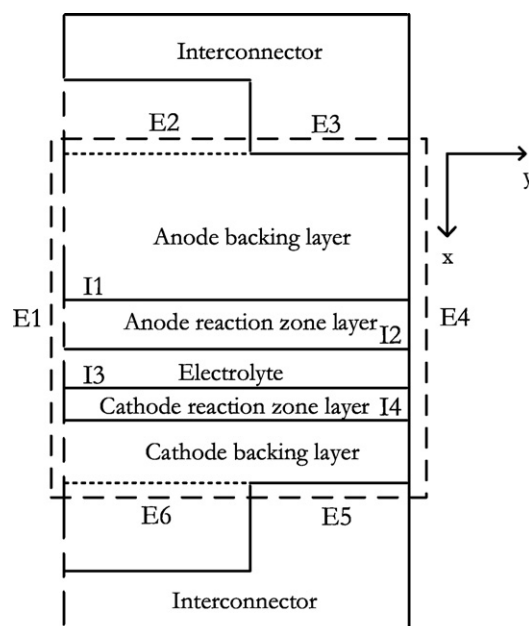

Fig. 1. Schematic of an anode-supported planar solid oxide fuel cell considered in this study.

species, which means the primary mode of species transport in the porous backing and reaction zone layers is by diffusion [5]. For instance, according to Yakabe [4], the calculated diffusion flux of H_2 at 1 A/cm² is about 0.23 mole/m²s, which is four orders of magnitude higher than convective flux (1×10^{-4} mole/m²s). The reactant gas mixtures are approximated as ideal gases with negligible Soret, Dofour and gravity effects. Since the reaction zone layers are considered as separate regions, there are no electrochemical reactions (either oxidation or reduction) in the backing layers. Moreover, in the present study, it is assumed that there is no electrochemical oxidation of CO in the anode reaction zone layer. In addition, the electrolyte layer is assumed to be a dense solid such that reactant gas crossover can be neglected. With these assumptions, the cell model is formulated and described in the following sections.

2.1. Backing Layers

Backing layers are porous structures, which provide flow paths for the reactants to and products from the reaction zone layers. They also conduct electrons through their solid portion, thereby providing a flow path for the transport of electrons. Therefore, the processes that need to be modeled in the backing layers are transport of multi-component mixture of species to and from the reaction zone layers along with chemical reactions (water-gas shift and methane reforming) in the anode backing layer, transport of electrons in the solid portion of the porous structures, and transfer of energy due to heat conduction, species diffusion and heat generation/consumption due to chemical reactions and electron migration.

The mathematical model governing the processes in the backing layers is formulated by applying conservation of species equation along with the modified Stefan–Maxwell equations incorporating Knudsen diffusion for multi-component gas diffusion, conservation of electronic charge, and conservation of energy. The governing equations are described as follows:

$$\text{Species}: \quad \nabla \cdot \vec{N}_i = \dot{S}_{s,i} \tag{1}$$

$$\text{Electronic charge}: \quad \nabla \cdot \vec{J}_e = 0 \tag{2}$$

$$\text{Energy}: \quad \nabla \cdot \vec{q} = \dot{S}_e \tag{3}$$

where $i \equiv CH_4$, H_2, H_2O, CO, and CO_2 for anode; and $i \equiv O_2$, and N_2 for cathode, $\vec{N}_i$ is the molar diffusion flux of species i, $\dot{S}_{s,i}$ is the species source term, $\vec{J}_e$ is the electronic current density, $\vec{q}$ is the energy flux, and $\dot{S}_e$ is the energy source term.

The diffusion flux in the porous layers can be determined using the modified Stefan–Maxwell equations incorporating Knudsen diffusion for multi-component systems involving n species [19]:

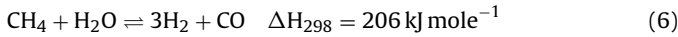$$\nabla x_i = \sum_{j=1}^{n} \frac{1}{c\mathcal{D}_{ij}^{\text{eff}}}(x_i \vec{N}_j - x_j \vec{N}_i) \tag{4}$$

where c is the concentration of the mixture, x_i is the mole fraction of species i, $\vec{N}_i$ is the diffusion flux of species i, and $\mathcal{D}_{ij}^{\text{eff}}$ is the effective diffusion coefficient, defined as

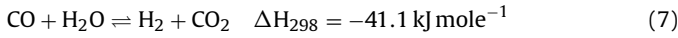$$\mathcal{D}_{ij}^{\text{eff}} = \frac{\varepsilon}{\tau}\left(\frac{D_{ij}D_{Kn,i}}{D_{ij} + D_{Kn,i}}\right) \tag{5}$$

where D_{ij} is the ordinary or binary diffusion coefficient and $D_{Kn,i}$ is the Knudsen diffusion coefficient of species i, ε and τ are porosity and tortuosity of the porous layers, respectively.

Since there is no chemical reaction in the cathode backing layer, the species source term in Eq. (1) corresponds to zero; whereas, in the anode backing layer, the species source term represents the rate of production or consumption of species due to methane reforming and water–gas shift reactions, as given below:

Methane reforming reaction:

$$CH_4 + H_2O \rightleftharpoons 3H_2 + CO \quad \Delta H_{298} = 206 \text{ kJ mole}^{-1} \tag{6}$$

Water–gas shift reaction:

$$CO + H_2O \rightleftharpoons H_2 + CO_2 \quad \Delta H_{298} = -41.1 \text{ kJ mole}^{-1} \tag{7}$$

The volumetric reaction rates for the above reactions can be written as

$$r_r = k_{fr}p_{CH_4}p_{H_2O} - k_{br}p_{H_2}^3 p_{CO} \tag{8}$$

$$r_s = k_{fs}p_{CO}p_{H_2O} - k_{bs}p_{CO_2}p_{H_2} \tag{9}$$

where r_r and r_s are volumetric reaction rates for the methane reforming and water–gas shift reactions expressed in mole m^{-3} s^{-1}, k_{fr} and k_{br} are the forward and backward reaction rate constants for the reforming reaction and k_{fs} and k_{bs} are the forward and backward reaction rate constants for the water–gas shift reaction, respectively. In terms of mole fractions, Eqs. (8) and (9) can be written as

$$r_r = p^2[k_{fr}x_{CH_4}x_{H_2O} - p^2 k_{br}x_{H_2}^3 x_{CO}] \tag{10}$$

$$r_s = p^2[k_{fs}x_{CO}x_{H_2O} - k_{bs}x_{CO_2}x_{H_2}] \tag{11}$$

where p is the total pressure. The equilibrium constants for the methane reforming and water–gas shift reactions can be determined from the following empirical relations [20]:

$$K_{pr} \equiv \frac{k_{fr}}{k_{br}} = 1.0267 \times 10^{10} \times \exp(-0.2513\zeta^4 + 0.3665\zeta^3$$
$$+ 0.5810\zeta^2 - 27.134\zeta + 3.2770) \tag{12}$$

$$K_{ps} \equiv \frac{k_{fs}}{k_{bs}} = \exp(-0.2935\zeta^3 + 0.635\zeta^2 + 4.1788\zeta + 0.3169) \tag{13}$$

where

$$\zeta = \frac{1000}{T(K)} - 1 \tag{14}$$

The forward reaction rate constants for the methane reforming and water–gas shift reactions are given as [20]:

$$k_{fr} = 2395 \exp\left(-\frac{231,266}{RT}\right) \quad (\text{mole m}^{-3}\text{ Pa}^{-2}\text{ s}^{-1}) \tag{15}$$

$$k_{fs} = 0.0171 \exp\left(-\frac{103,191 \text{ J mole}^{-1}}{RT}\right) \quad (\text{mole m}^{-3}\text{ Pa}^{-2}\text{ s}^{-1}) \tag{16}$$

where R is the universal gas constant and T is the temperature.

Knowing the forward reaction rate constants and equilibrium constants for the methane reforming and water–gas shift reactions, the backward reaction rate constants can be obtained using the first equality in Eqs. (12) and (13).

Finally, the rates of production or consumption of various species in the anode backing layer can be formulated as follows:

$$\dot{S}_{s,CH_4} = -r_r \tag{17}$$

$$\dot{S}_{s,H_2} = 3r_r + r_s \tag{18}$$

$$\dot{S}_{s,H_2O} = -r_r - r_s \tag{19}$$

$$\dot{S}_{s,CO} = r_r - r_s \tag{20}$$

$$\dot{S}_{s,CO_2} = r_s \tag{21}$$

Using Ohm's law, the electronic current density given in Eq. (2) can be written in terms of electronic potential, then the conservation of charge in the backing layers becomes

Electronic charge : $\quad \nabla \cdot (\sigma_{bl}^{\text{eff}}\nabla \phi_e) = 0 \tag{22}$

where σ_{bl}^{eff} is the effective electronic conductivity of the backing layers, defined as

$$\sigma_{bl}^{\text{eff}} = \left(\frac{1-\varepsilon}{\tau}\right)\sigma \tag{23}$$

where ε and τ are the porosity and tortuosity of the porous backing layers, respectively, and σ is the electronic conductivity of the pure backing layer material (or the bulk electronic conductivity).

The heat flux $\vec{q}$ in Eq. (3) accounts for the contributions resulting from interdiffusion of multi-component mixture in addition to the conductive flux, which is expressed as

$$\vec{q} = -k_{bl}^{\text{eff}}\nabla T + \sum_{i=1}^{n} h_i \vec{N}_i \tag{24}$$

where h_i is the absolute enthalpy of the species i, and k_{bl}^{eff} is the effective thermal conductivity of the backing layers, defined as

$$k_{bl}^{\text{eff}} = \varepsilon k_f + (1-\varepsilon)k_s \tag{25}$$

where k_f is the thermal conductivity of fluid mixture in the backing layers and k_s is the thermal conductivity of the solid phase of the porous backing layers. The thermal conductivity of the multi-component fluid mixture is obtained as [21]

$$k_f = \sum_{i=1}^{n} \frac{x_i k_i}{\left(\sum_{j=1}^{n} x_j \Phi_{ij}\right)} \tag{26}$$

where x_i is the mole fraction of species i in a mixture, k_i is the thermal conductivity of the pure component i, and Φ_{ij} is defined as

$$\Phi_{ij} = \frac{1}{\sqrt{8}}\left(1 + \frac{M_i}{M_j}\right)^{-(1/2)}\left[1 + \left(\frac{\mu_i}{\mu_j}\right)^{1/2}\left(\frac{M_j}{M_i}\right)^{1/4}\right]^2 \tag{27}$$

where M_i is the molecular weight of species i, and μ_i is the dynamic viscosity of pure component i.

The energy source term in Eq. (3) accounts for Joule heating effect representing the resistance to electron flow in the solid phase of porous backing layers and energy generation or consumption

Table 1
Governing equations in the backing layers.

Governing equations	Anode backing layer	Cathode backing layer
Species	$\nabla \cdot \vec{N}_i = \dot{S}_{s,i}$	$\nabla \cdot \vec{N}_i = 0$
Modified S-M	$\nabla x_i = \sum_{j=1}^{n} \frac{1}{cD_{ij}^{eff}}(x_i \vec{N}_j - x_j \vec{N}_i)$	$\nabla x_i = \sum_{j=1}^{n} \frac{1}{cD_{ij}^{eff}}(x_i \vec{N}_j - x_j \vec{N}_i)$
Electronic charge	$\nabla \cdot \left(\sigma_{bl}^{eff} \nabla \phi_e \right) = 0$	$\nabla \cdot \left(\sigma_{bl}^{eff} \nabla \phi_e \right) = 0$
Energy	$\nabla \cdot \left(k_{bl}^{eff} \nabla T \right) - \left(\sum_{i=1}^{n} c_{pi} \vec{N}_i \right) \cdot \nabla T + \frac{J_e^2}{\sigma_{bl}^{eff}} - \left(\sum_{i=1}^{n} h_i \dot{S}_{s,i} \right) = 0$	$\nabla \cdot \left(k_{bl}^{eff} \nabla T \right) - \left(\sum_{i=1}^{n} c_{pi} \vec{N}_i \right) \cdot \nabla T + \frac{J_e^2}{\sigma_{bl}^{eff}} = 0$

due to chemical reactions in the anode backing layer, which can be expressed as

$$\dot{S}_e = \frac{J_e^2}{\sigma_{bl}^{eff}} \tag{28}$$

Substituting the expressions of energy flux and energy source term in Eq. (3), the final form of energy equation in the backing layers becomes

$$\nabla \cdot \left(k_{bl}^{eff} \nabla T \right) - \left(\sum_{i=1}^{n} c_{pi} \vec{N}_i \right) \cdot \nabla T + \frac{J_e^2}{\sigma_{bl}^{eff}} - \left(\sum_{i=1}^{n} h_i \dot{S}_{s,i} \right) = 0 \tag{29}$$

where c_{pi} is the specific heat at constant pressure for the species i.

It is worthwhile to mention that the last term on the left-hand side of above equation vanishes for cathode backing layer since there is no chemical reaction in the cathode. The governing equations in the backing layers are summarized in Table 1.

2.2. Reaction zone layers

Reaction zone layers are relatively thin layers having thicknesses of the order of 10 μm. These are the regions where fuel and oxidant are electrochemically converted into electrical work, heat and water vapor. Since both electron- and ion-conducting particles co-exist with reactant species, these regions can be treated as composite electrodes.

Reaction zone layers have been modeled as thin film models, random resistor network models, random packing sphere models or macroscopic porous-electrode models, respectively. The thin film models [22,23] are based on the assumption that the three phases of reaction zone layers (i.e., electronic, ionic, and gas) form straight paths from the electrolyte to the backing layers. Because of this assumption in thin film models, the reaction zone layers are represented by a very ordered structure in place of highly disordered structure as observed in the experimental features of composite electrodes [15]. In random resistor network models [24,25], the composite electrode is assumed to consists of electron- and ion-conducting particles packed together to form a continuous network. These models involve storage of information in terms of individual particle locations and connectivity with other particles to construct resistor networks, followed with calculation of electric potential at each particle location. Due to high computational costs, the use of random resistor network models is limited to problems with small specimen size [7]. In random packing sphere models [13,14,41], the composite electrode is assumed to be spherical particles of electron- and ion-conducting materials packed together at random. Due to randomness of these models, the random resistor network models and random packing sphere models are also referred to as Monte Carlo resistor network models and Monte Carlo packing sphere models, respectively. On the other hand, macroscopic porous-electrode models are based on the assumption that the composite electrode is represented by the particles of electron- and ion-conducting materials packed together at random and disregards the actual geometric details of the individual particles. Instead, the

composite electrode is described in terms of continuous-average quantities. Hence, in the present model, the macroscopic porous-electrode approach is used to model reaction zone layers, which according to Sunde [15] is the most practical method for applied research.

The processes that need to be modeled in the reaction zone layers are transport of multi-component mixture of species to and from the reaction sites along with chemical (water–gas shift and methane reforming) and electrochemical reactions, respectively transport of electrons and ions in the electron- and ion-conducting particles, and transfer of energy due to heat conduction, species diffusion, heat generation/consumption due to chemical and electrochemical reactions and electron and ion migration.

The conservation of species equation governing the transport of multi-component mixture in the reaction zone layers is similar to the backing layers given in Eq. (1) except the source term, which accounts for the consumption or production of species due to electrochemical reactions in addition to the chemical reactions described in the anode backing layer. Again, the modified Stefan–Maxwell equations given in Eq. (4) are used to model the diffusion flux in the reaction zone layers. The equations governing the transport of electrons and oxide ions in the electron- and ion-conducting particles of the reaction zone layers are described as follows;

Anode reaction zone layer:

Electronic charge : $\quad \nabla \cdot \vec{J}_e = \mathcal{R}_a$ (30)

Ionic charge : $\quad \nabla \cdot \vec{J}_i = -\mathcal{R}_a$ (31)

Cathode reaction zone layer:

Electronic charge : $\quad \nabla \cdot \vec{J}_e = -\mathcal{R}_c$ (32)

Ionic charge : $\quad \nabla \cdot \vec{J}_i = \mathcal{R}_c$ (33)

where $\mathcal{R}_a$ and $\mathcal{R}_c$ are the volumetric current densities produced in the anode and cathode reaction zone layers due to H_2 oxidation and O_2 reduction reactions, respectively, which are represented by the general Butler–Volmer equations, expressed as

$$\mathcal{R}_a = A_v J_{0,ref}^{H_2} \left(\frac{c_{H_2}}{c_{H_2,ref}} \right)^{\gamma_{H_2}} \left\{ \exp\left(\frac{\alpha n F \eta}{RT} \right) - \exp\left(-\frac{(1-\alpha)nF\eta}{RT} \right) \right\} \tag{34}$$

$$\mathcal{R}_c = A_v J_{0,ref}^{O_2} \left(\frac{c_{O_2}}{c_{O_2,ref}} \right)^{\gamma_{O_2}} \left\{ \exp\left(-\frac{\alpha n F \eta}{RT} \right) - \exp\left(\frac{(1-\alpha)nF\eta}{RT} \right) \right\} \tag{35}$$

where A_v is the actual reactive surface area per unit volume, $J_{0,ref}^{H_2}$ and $J_{0,ref}^{O_2}$ are the reference exchange current densities for H_2 oxidation and O_2 reduction reactions at reference concentrations $c_{H_2,ref}$ and $c_{O_2,ref}$, respectively, α is the charge transfer coefficient (or symmetry factor), whose value lies between zero and one, n is the number of electrons participating in the electrochemical reaction and η is the electrode activation overpotential (anode or cathode), defined as

$$\eta = \phi_i - \phi_e \tag{36}$$

In order to enhance the predictive capability of the model, the expression used to model the reactive surface area per unit volume is based on random packing of binary spherical particles developed by Costamagna and Honegger [41], which is given as

$$A_v = \pi \sin^2 \theta r_{el}^2 n_t n_{el} n_{io} \frac{Z_{el} Z_{io}}{Z} p_{el} p_{io} \tag{37}$$

where θ is the contact angle between the electron- and ion-conducting particles in the reaction zone layers, r_{el} is the radius of the electron-conducting particles, n_t is the total number of particles per unit volume, n_{el} and n_{io} are the number fractions of the electron- and ion-conducting particles in the reaction zone layers, respectively, Z_{el} and Z_{io} are the coordination numbers of the electron- and ion-conducting particles in the reaction zone layers, respectively, Z is the total average number of contacts of each particle and p_{el} and p_{io} are the probabilities of the electron- and ion-conducting particles in the reaction zone layers, respectively.

The parameters required to obtain the reactive surface area per unit volume (A_v) are calculated using the following expressions [41,15]:

$$n_t = \frac{1 - \epsilon}{(4/3)\pi r_{el}^3 [n_{el} + (1 - n_{el})(r_{io}/r_{el})^3]} \tag{38}$$

where ϵ is the porosity of the reaction zone layers:

$$n_{el} = \frac{\Phi}{[\Phi + ((1 - \Phi)/(r_{io}/r_{el})^3)]} \tag{39}$$

where Φ is the volume fraction of the electron-conducting particles in the reaction zone layers:

$$Z_{el} = 3 + \frac{(Z - 3)}{[n_{el} + (1 - n_{el})(r_{io}/r_{el})^2]} \tag{40}$$

$$Z_{io} = 3 + \frac{(Z - 3)(r_{io}/r_{el})^2}{[n_{el} + (1 - n_{el})(r_{io}/r_{el})^2]} \tag{41}$$

where Z is the total average coordination number, equal to 6 [15]:

$$p_{el} = [1 - (2 - Z_{el-el}/2)^{2.5}]^{0.4} \tag{42}$$

$$p_{io} = [1 - (2 - Z_{io-io}/2)^{2.5}]^{0.4} \tag{43}$$
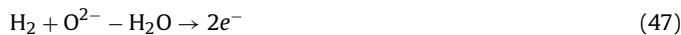
where

$$Z_{el-el} = \frac{n_{el} Z_{el}^2}{Z} \tag{44}$$

$$Z_{io-io} = \frac{n_{io} Z_{io}^2}{Z} \tag{45}$$

The species source terms in the anode and cathode reaction zone layers due to electrochemical reactions are related to volumetric current density produced through Faraday's law of electrochemical reaction, and are described as follows:
Anode reaction zone layer:

$$\dot{S}_{s,H_2} = -\frac{\nu_{H_2} \mathcal{R}_a}{nF} \tag{46}$$

where $\mathcal{R}_a$ is the volumetric current density produced due to H_2 oxidation reaction given in Eq. (34), n is the number of electrons participating in the electrochemical reaction, F is the Faraday's constant, and ν_{H_2} is the stoichiometric coefficient of the H_2 involved in the oxidation reaction expressed in the following form [26]:

$$H_2 + O^{2-} - H_2O \rightarrow 2e^- \tag{47}$$

Cathode reaction zone layer:

$$\dot{S}_{s,O_2} = -\frac{\nu_{O_2} \mathcal{R}_c}{nF} \tag{48}$$

where $\mathcal{R}_c$ is the volumetric current density produced due to O_2 reduction reaction given in Eq. (35), and ν_{O_2} is the stoichiometric coefficient of the O_2 involved in the reduction reaction expressed in the following form [26]:

$$\frac{1}{2}O_2 - O^{2-} \rightarrow 2e^- \tag{49}$$

Expressing the electronic and ionic current densities in terms of electronic and ionic potentials through Ohm's law, Eqs. (30)–(33) become
Anode reaction zone layer:

Electronic charge : $\nabla \cdot (\sigma_{rl}^{\text{eff}} \nabla \phi_e) = -\mathcal{R}_a \tag{50}$

Ionic charge : $\nabla \cdot (\kappa_{rl}^{\text{eff}} \nabla \phi_i) = \mathcal{R}_a \tag{51}$

Cathode reaction zone layer:

Electronic charge : $\nabla \cdot (\sigma_{rl}^{\text{eff}} \nabla \phi_e) = \mathcal{R}_c \tag{52}$

Ionic charge : $\nabla \cdot (\kappa_{rl}^{\text{eff}} \nabla \phi_i) = -\mathcal{R}_c \tag{53}$

where the effective electronic and ionic conductivities in the reaction zone layers are determined as follows:

$$\sigma_{rl}^{\text{eff}} = \Phi \left(\frac{1 - \epsilon}{\tau} \right) \sigma \tag{54}$$

$$\kappa_{rl}^{\text{eff}} = (1 - \Phi) \left(\frac{1 - \epsilon}{\tau} \right) \kappa \tag{55}$$

where Φ is the volume fraction of the electron-conducting particles in the reaction zone layers, σ and κ are the conductivities of pure electron- and ion-conducting materials, respectively.

The conservation of energy equation in the reaction zone layers is similar to the backing layers except the energy source term, which is expressed as

$$\nabla \cdot (k_{rl}^{\text{eff}} \nabla T) - \left(\sum_{i=1}^{n} c_{pi} \vec{N}_i \right) \cdot \nabla T - \left(\sum_{i=1}^{n} h_i \dot{S}_{s,i} \right) + \dot{S}_e = 0 \tag{56}$$

where k_{rl}^{eff} is the effective thermal conductivity of the reaction zone layer, calculated as

$$k_{rl}^{\text{eff}} = \varepsilon k_f + (1 - \varepsilon)[\Phi k_{el} + (1 - \Phi)k_{io}] \tag{57}$$

where k_f is the thermal conductivity of the fluid mixture in the reaction zone layers obtained using Eq. (26), Φ is the volume fraction of the electron-conducting particles in the reaction zone layers, k_{el} and k_{io} are the thermal conductivities of pure electron- and ion-conducting materials, respectively.

The energy source term $\dot{S}_e$ in the reaction zone layers is represented as
Anode reaction zone layer:

$$\dot{S}_e = \frac{|J_e^2|}{\sigma_{rl}^{\text{eff}}} + \frac{|J_i^2|}{\kappa_{rl}^{\text{eff}}} + \left| \frac{\mathcal{R}_a}{nF} \right| (-T(\Delta \bar{s})_{H_2,ox}) + \mathcal{R}_a \eta \tag{58}$$

where the first term on the right-hand side (RHS), $(|J_e^2|)/(\sigma_{rl}^{\text{eff}})$, represents the Joule heating effect due to the resistance to the electron flow in the electron-conducting particles of the anode reaction zone layer, the second term, $(|J_i^2|)/(\kappa_{rl}^{\text{eff}})$, represents the Joule heating effect due to the resistance to the ion flow in the ion-conducting particles of the anode reaction zone layer, the third term, $(|\mathcal{R}_a/nF|(-T(\Delta \bar{s})_{H_2,ox}))$, represents the reversible heat generation due to the electrochemical H_2 oxidation reaction, and the last term, $\mathcal{R}_a \eta$, represents the irreversible heat generation due to electrochemical H_2 oxidation reaction.

In order to find the reversible heat generation due to the electrochemical reaction in the anode reaction zone layer, the entropy change between the reactants and the products has to be determined. However, the entropy of formation for the ions and electrons are not known. Therefore, the entropy change for an overall SOFC

Table 2
Governing equations in the reaction zone layers.

Governing equations	Anode reaction zone layer	Cathode reaction zone layer
Species	$\nabla \cdot \overline{N}_i = \dot{S}_{s,i}$	$\nabla \cdot \overline{N}_i = \dot{S}_{s,O_2}$
Modified S-M	$\nabla x_i = \sum_{j=1}^n \frac{1}{c\mathcal{D}_{ij}^{\text{eff}}} \left(x_i \overline{N}_j - x_j \overline{N}_i \right)$	$\nabla x_i = \sum_{j=1}^n \frac{1}{c\mathcal{D}_{ij}^{\text{eff}}} \left(x_i \overline{N}_j - x_j \overline{N}_i \right)$
Electronic Charge	$\nabla \cdot \left(\sigma_{rl}^{\text{eff}} \nabla \phi_e \right) = -\mathcal{R}_a$	$\nabla \cdot \left(\sigma_{rl}^{\text{eff}} \nabla \phi_e \right) = \mathcal{R}_c$
Ionic Charge	$\nabla \cdot \left(\kappa_{rl}^{\text{eff}} \nabla \phi_i \right) = \mathcal{R}_a$	$\nabla \cdot \left(\kappa_{rl}^{\text{eff}} \nabla \phi_r \right) = -\mathcal{R}_c$
Energy	$\nabla \cdot \left(k_{rl}^{\text{eff}} \nabla T \right) - \left(\sum_{i=1}^n c_{pi} \overline{N}_i \right) \cdot \nabla T + \frac{J_e^2}{\sigma_{rl}^{\text{eff}}} + \frac{J_i^2}{\kappa_{rl}^{\text{eff}}} +$ $\left\| \frac{\mathcal{R}_a}{nF} \right\| \left(-T\xi_{H_2}(\Delta\bar{s})_{H_2} \right) + \mathcal{R}_a\eta - \left(\sum_{i=1}^n h_i \dot{S}_{s,i} \right) = 0$	$\nabla \cdot \left(k_{rl}^{\text{eff}} \nabla T \right) - \left(\sum_{i=1}^n c_{pi} \overline{N}_i \right) \cdot \nabla T + \frac{J_e^2}{\sigma_{rl}^{\text{eff}}} + \frac{J_i^2}{\kappa_{rl}^{\text{eff}}} +$ $\left| \frac{\mathcal{R}_c}{nF} \right| \left(-T(1-\xi_{H_2})(\Delta\bar{s})_{H_2} \right) + \mathcal{R}_c\eta = 0$

reaction is determined in place of overall half-cell reactions. The overall SOFC reaction is

$$H_2 + \frac{1}{2}O_2 \rightleftharpoons H_2O_{(g)} \tag{59}$$
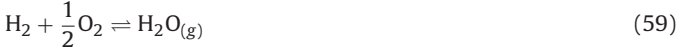
The change in entropy between the products and reactants for the above overall SOFC reaction is

$$(\Delta\bar{s})_{H_2} = \bar{s}_{H_2O} - \bar{s}_{H_2} - \frac{1}{2}\bar{s}_{O_2} \tag{60}$$

The entropy change in the anode reaction zone layer during the H_2 oxidation reaction is assumed to be a fraction of the entropy change for the overall SOFC reaction, so that

$$\dot{S}_e = \frac{|J_e^2|}{\sigma_{rl}^{\text{eff}}} + \frac{|J_i^2|}{\kappa_{rl}^{\text{eff}}} + \left| \frac{\mathcal{R}_a}{nF} \right| (-T\xi_{H_2}(\Delta\bar{s})_{H_2}) + \mathcal{R}_a\eta \tag{61}$$

where ξ_{H_2} is the fraction of the entropy change for the overall SOFC reaction of H_2.

Cathode reaction zone layer:

$$\dot{S}_e = \frac{|J_e^2|}{\sigma_{rl}^{\text{eff}}} + \frac{|J_i^2|}{\kappa_{rl}^{\text{eff}}} + \left| \frac{\mathcal{R}_c}{nF} \right| [-T(1-\xi_{H_2})(\Delta\bar{s})_{H_2}] + \mathcal{R}_c\eta \tag{62}$$

where the first term on the right-hand side, $(|J_e^2|)/(\sigma_{rl}^{\text{eff}})$, represents the Joule heating effect due to the resistance to the electron flow in the electron-conducting particles of the cathode reaction zone layer, the second term, $(|J_i^2|)/(\kappa_{rl}^{\text{eff}})$, represents the Joule heating effect due to the resistance to the ion flow in the ion-conducting particles of the cathode reaction zone layer, the third term, $(|\mathcal{R}_c/nF|(-T(1-\xi_{H_2})(\Delta\bar{s})_{H_2,ox}))$, represents the reversible heat generation due to the electrochemical O_2 reduction reaction, and the last term, $\mathcal{R}_c\eta$, represents the irreversible heat generation due to the electrochemical O_2 reduction reaction. The governing equations in the reaction zone layers are summarized in Table 2.

2.3. Electrolyte layer

The electrolyte layer in SOFC is fully dense with no interconnected porosity. The function of the electrolyte layer is to conduct oxide ions produced in the cathode reaction zone layer to the anode reaction zone layer, thus completing the electrical circuit. The processes which need to be modeled are the transport of oxide ions and transfer of energy due to heat conduction and heat generation due to ion migration. The conservation equation governing the processes in the electrolyte layer are given as

$$\text{Ionic charge}: \quad \nabla \cdot \overrightarrow{J}_i = 0 \tag{63}$$

$$\text{Energy}: \quad \nabla \cdot \overrightarrow{q} = \dot{S}_e \tag{64}$$

where $\overrightarrow{J}_i$ is the ionic current density, which is equal to the cell current density $\overrightarrow{J}$, and $\dot{S}_e$ is the energy source term due to the resistance to the transport of oxide ions, which is expressed as

$$\dot{S}_e = \frac{J^2}{\kappa} \tag{65}$$

where κ is the ionic conductivity of the electrolyte.

Using Ohm's law and Fourier's law of heat conduction, the ionic current density and heat flux are expressed in terms of the ionic potential and temperature, respectively; the above conservation equations become

$$\text{Ionic charge}: \quad \nabla \cdot (\kappa \nabla \phi_i) = 0 \tag{66}$$

$$\text{Energy}: \quad \nabla \cdot (k_{ele} \nabla T) + \frac{J^2}{\kappa} = 0 \tag{67}$$

where κ and k_{ele} are the ionic and thermal conductivities of the electrolyte, respectively. The governing equations in the electrolyte layer are summarized in Table 3.

2.4. Boundary conditions

Since SOFC modeling involves interdependent transport processes in different components, the specification of boundary conditions includes both external and internal boundary conditions [27]. The locations at which boundary conditions are required in the model are illustrated in the schematic shown in Fig. 1. The locations of the external boundary conditions are represented by E1–E6; whereas, the locations of the internal boundary conditions are represented by I1–I4. Since a planar SOFC is symmetric about the middle of the flow channel, symmetric boundary conditions are applied at E1. The boundaries E2 and E6 represent the interfaces between the gas flow channels and the backing layers, where composition of gaseous species are specified, electronic current densities are insulated, and the temperature at these boundaries is specified as the inlet temperatures of gas streams. The boundaries E3 and E5 represent the land portions of the interconnects which are in contact with the backing layers, where the mass fluxes of species are zero, electronic potential is set as ground potential at boundary E3, and either cell potential or current density is specified at boundary E5 depending upon the approach used in the particular simulation. Since the computational domain only includes the land portions of the interconnects, the temperatures are specified at boundaries E3 and E5 as first approximations, instead of continuous heat flux boundary conditions, which are applicable when the interconnects are included in the computational domain. The boundary E4 represents the external boundary, where insulated boundary conditions are applicable, which means the molar flux of species, current densities (electronic and ionic), and heat flux are zero.

The internal boundaries I1 and I4 represent the interfaces between the backing and reaction zone layers. The boundary conditions at these boundaries are continuous flux boundary conditions for the species and electronic potential, where the molar flux

Table 3
Governing equations in the electrolyte layer.

Governing equations	Electrolyte layer
Ionic charge	$\nabla \cdot (\kappa \nabla \phi_i) = 0$
Energy	$\nabla \cdot (k_{ele} \nabla T) + \frac{J^2}{\kappa} = 0$

Table 4
Boundary conditions.

Boundary/internal locations	Conditions
E1	$\frac{\partial x_i}{\partial y} = \frac{\partial \phi_e}{\partial y} = \frac{\partial \phi_i}{\partial y} = \frac{\partial T}{\partial y} = 0$
E2 and E6	$x_i = \text{specified}; \vec{J}_e \cdot \vec{n} = 0; T = \text{specified}$
E3	$\vec{N}_i \cdot \vec{n} = 0; \phi_e = 0; T = \text{specified}$
E4	$\vec{N}_i \cdot \vec{n} = \vec{J}_e \cdot \vec{n} = \vec{J}_i \cdot \vec{n} = \vec{q} \cdot \vec{n} = 0$
E5	$\vec{N}_i \cdot \vec{n} = 0; \vec{J}_e \cdot \vec{n} = J; T = \text{specified}$
I1 and I4	$\vec{N}_i \cdot \vec{n}\|_{bl} = \vec{N}_i \cdot \vec{n}\|_{rl}; \vec{J}_e \cdot \vec{n}\|_{bl} = \vec{J}_e \cdot \vec{n}\|_{rl}$
	$\vec{J}_i \cdot \vec{n}\| = 0; \vec{q} \cdot \vec{n}\|_{bl} = \vec{q} \cdot \vec{n}\|_{rl}$
I2 and I3	$\vec{N}_i \cdot \vec{n} = 0; \vec{J}_e \cdot \vec{n} = 0; \vec{J}_i \cdot \vec{n} = J$
	$\vec{q} \cdot \vec{n}\|_{rl} = \vec{q} \cdot \vec{n}\|_{el}$

and electronic current density are continuous; whereas, insulated boundary condition applies for the ionic potential, which implies ionic current density is zero. The interfaces between the reaction zone layers and the electrolyte layer are represented by I2 and I3. Since the electrolyte is an electron insulator with no interconnected porosity, the molar flux of species and electronic current density are zero at these interface boundaries. Whereas, the boundary condition for the ionic potential depends on the approach used in fuel cell modeling. As it is known in fuel cell modeling, either current density is specified to obtain the cell potential or vice versa. When current density is specified, the ionic current density at these boundaries (I2 and I3) is set equal to the cell current density; however, when cell potential is specified to obtain the current density, the ionic current density at these boundaries (I2 and I3) is continuous. Similarly, the heat flux is continuous at these boundaries irrespective of the approaches used. Finally, the boundary conditions expressed in mathematical form are summarized in Table 4.

3. Numerical implementation

The governing equations tabulated in Tables 1– 3 need to be discretized to obtain the numerical solution. Since the mathematical model governing the processes in different layers of an SOFC is based on the conservation principle, the discretization scheme commonly used for problems involving conservative laws is a well-known method, often referred to as finite volume method or control volume method [28,29]. The application of finite volume method to fuel cell related problems has already been recognized by various researchers [30,31].

The governing discretized equations form a system of algebraic equations, whose solution can be obtained using a direct or an iterative method. For the present problem, which is highly non-linear, involving interdependent variables with multi-component mixture of species, an iterative solver is used to obtain the solution of the discretized governing equations.

The grid (numerical mesh) is uniform locally but non-uniform globally, which means the mesh size is uniform within a layer or component of the computational domain. Finer mesh sizes are used in the reaction zone layers than in the backing layers to capture the electrochemical reactions and other processes. Grid sensitivity tests are performed to ensure grid independent solution. For instance, beyond the grid size of 150×50, no significant change is observed in the species distribution in different layers of the cell.

4. Model validation

Model validation is as important as model development. It helps in determining the range of validity and accuracy of the model. However, only few researchers [4,5,32] have shown the validation of their SOFC models. The parameters used in the validation of the present model are listed in Table 5. Most of the parameters are

Table 5
Parameters used for model validation.

Operating temperature, T_{op} (K)	1023.0
Total pressure, p (atm)	1.0
Reference fuel composition, x_{H_2}; x_{H_2O}	0.8; 0.2
Anode electrode layer thickness, t_a (μm)	1950.0
Anode reaction zone layer thickness, t_{arz} (μm)	50.0 [11]
Resistivity of electron-conducting particles, ρ_{el} (Ωm),	$2.98 \times 10^{-5} \exp\left(-\frac{1332}{T}\right)$ [33]
Resistivity of ion-conducting paricles, ρ_{io} (Ωm),	$2.94 \times 10^{-5} \exp\left(\frac{10350}{T}\right)$ [33]
Porosity, ε	0.46
Tortuosity, τ	4.5
Pore diameter, d_p (μm)	2.6
Contact angle between electron- and ion-conducting particles, θ	15° [41]
Radius of electron-conducting particles, r_{el} (μm)	0.1 [13,15]
Radius of ion-conducting particles, r_{io} (μm)	0.1 [13,15]
Volume fraction of electron-conducting particles, Φ	0.5 [12,15]
Reference H_2 concentration, c_{H_2} (mole m^{-3})	10.78
Reference exchange current density for H_2 oxidation, $J_{0,ref}^{H_2}$ (A m^{-2})	1320 [5]
Reaction order for H_2 oxidation, γ_{H_2}	0.5

Source: Yakabe et al. [4].

obtained from Yakabe et al. [4], who reported the measured data for concentration overpotential for a ternary mixture at different current densities. The thickness of the anode is reported to be 2 mm, of which 50 μm is treated as the thickness of the anode reaction zone layer, which is in accordance with the depth of the reaction zone reported by Lehnert et al. [11] for an anode thickness of 2 mm.

Fig. 2 shows the comparison between the model prediction and measured data at 0.7 A cm^{-2}. The abscissa of Fig. 2 represents the variation in reactant concentration, while the ordinate represents the difference between the actual and reference concentration overpotential. The reference concentration overpotential was measured when there was no argon in the system at hydrogen mole fraction equal to 0.8. Argon was added to the system to vary the reactant concentration such that the ratio of the mole fractions of hydrogen and water vapor is 4:1. It can be seen that increasing the reactant concentration decreases the concentration overpotential difference.
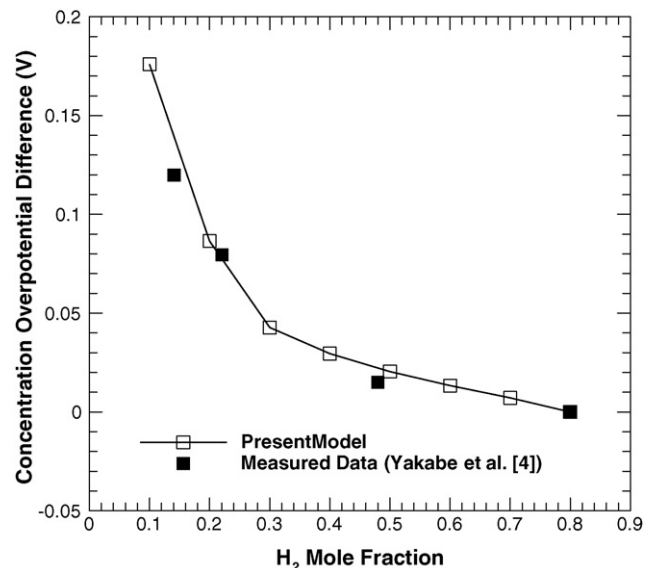

Fig. 2. Model validation.

Table 6
Fuel composition used in the simulation.

Species	Mole fraction
CH_4	0.171
H_2	0.263
H_2O	0.493
CO	0.029
CO_2	0.044

Source: Lehnert et al. [11].

Table 7
Base case parameters used in the simulation.

Operating temperature, T_{op} (K)	1073.0
Total pressure, p (atm)	1.0
Oxidant composition, x_{O_2}; x_{N_2}	0.21; 0.79
Anode backing layer thickness, t_a (μm)	1950.0
Anode reaction zone layer thickness, t_{arz} (μm)	50.0
Electroyte thickness, t_e (μm)	20.0
Cathode backing layer thickness, t_c (μm)	50.0
Cathode reaction zone layer thickness, t_{crz} (μm)	10.0
Resistivity of electron-conducting particles in anode, ρ_{el} (Ωm)	$2.98 \times 10^{-5} \exp\left(-\frac{1332}{T}\right)$ [33]
Resistivity of ion-conducting paricles, ρ_{io} (Ωm),	$2.94 \times 10^{-5} \exp\left(\frac{10350}{T}\right)$ [33]
Resistivity of electron-conducting particles in cathode, ρ_{el} (Ωm)	$8.11 \times 10^{-5} \exp\left(\frac{600}{T}\right)$ [33]
Thermal conductivity of electrodes, k_{el} (W m^{-1})	3 [34]
Thermal conductivity of electrolyte, k_{io} (W m^{-1})	2 [34]
Porosity, ε	0.3 [15]
Tortuosity, τ	4.5 [4,17]
Pore diameter, d_p (μm)	1.0 [5]
Contact angle between electron- and ion-conducting particles, θ	15° [41]
Radius of electron-conducting particles, r_{el} (μm)	0.1 [13,15]
Radius of ion-conducting particles, r_{io} (μm)	0.1 [13,15]
Volume fraction of electron-conducting particles, Φ	0.5 [12,15]
Reference H_2 concentration, c_{H_2} mole m^{-3}	10.78
Reference O_2 concentration, c_{O_2} mole m^{-3}	2.38
Reference exchange current density for H_2 oxidation, $J_{0,ref}^{H_2}$ A m^{-2}	1320 [5]
Reference exchange current density for O_2 oxidation, $J_{0,ref}^{O_2}$ A m^{-2}	200 [41]
Reaction order for H_2 oxidation, γ_{H_2}	0.5
Reaction order for O_2 oxidation, γ_{O_2}	0.5

This is due to increased reactant concentration at the reactant sites, which results in reducing the concentration overpotential. Further, it can be seen that the concentration overpotential difference predicted by the model is in excellent agreement with measured data. The coefficient of determination or R^2 value, an indicator between 0 and 1, reveals how closely the predicted values correspond to measured data, is obtained as 0.989.

5. Results and discussion

The developed model not only predicts the concentration overpotential but also predicts the activation and ohmic overpotentials, which in turn helps in predicting the overall performance of an anode-supported SOFC. The fuel composition and the base case parameters used in the simulation are listed in Tables 6 and 7, respectively.

Fig. 3 shows the cell performance resulting from the fuel composition and base case parameters listed in Tables 6 and 7, respectively. The abscissa of Fig. 3 represents the current density (load), whereas the primary (left) and secondary (right) ordinate represent the cell potential and power density, respectively. The solid line corresponds to the cell potential and power density when all the overpotentials are subtracted from the reversible cell potential. The overpotentials include anode overpotential, cathode overpotential and electrolyte overpotential. Anode and cathode overpotentials include activation overpotentials due to the resistance to the charge transfer reactions, ohmic overpotentials due to the resistance to the flow of electrons and ions in the reaction zone layers and the resistance to the flow of electrons in the backing layers, and concentration overpotentials due to the resistance to the flow of reactant species through the void spaces. Conversely, the dashed lines correspond to the cell potential when anode overpotential, electrolyte overpotential, and cathode overpotential are not

Fig. 3. Base case performance of anode-supported an SOFC.

included in obtaining the polarization curves. It can be seen that the solid line representing the actual overpotential exhibits regions of activation and concentration overpotentials at low and high current densities, respectively. Specifically, these regions of activation and concentration overpotentials are due to the cathode activation and anode concentration overpotentials, which is evident from the dashed lines neglecting cathode and anode overpotentials, respectively. Additionally, it is observed that the maximum power density obtained for an anode-supported SOFC using the fuel composition and base case parameters listed in Tables 6 and 7 is about 0.4 W cm^{-2}. It is worthwhile to note that the average values of activation overpotentials are used in obtaining the polarization curves, since the values of activation overpotentials vary within the reaction zone layers with maximum at the interface between the reaction zone and electrolyte layers and minimum at the interface between the backing and reaction zone layers.

It is also seen from Fig. 3 that the profiles without the anode and cathode overpotentials exhibit almost similar performances for current density upto about 1 A cm^{-2}, indicating comparable magnitudes of anode and cathode overpotentials. However, at current densities beyond 1 A cm^{-2}, the profile without the anode overpotential shows better performance. The reason for better performance at higher current densities is because of anode concentration overpotential, which is not included in the profile without anode overpotential. Further, it is observed that the contribution of electrolyte overpotential is not negligible even though its thickness is negligible relative to the thickness of the anode. To better understand these observations, the anode overpotentials at the base case condition are further investigated, and a typical result is shown in Fig. 4. It is clear that the ohmic overpotential is the single largest contributor to the overall anode overpotential and the
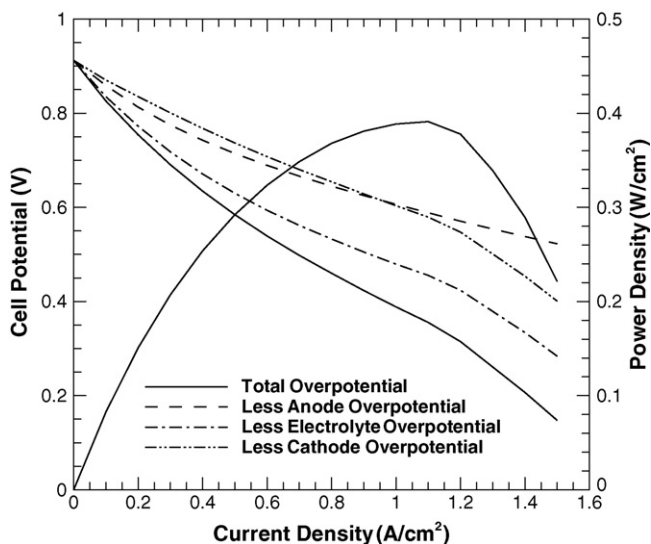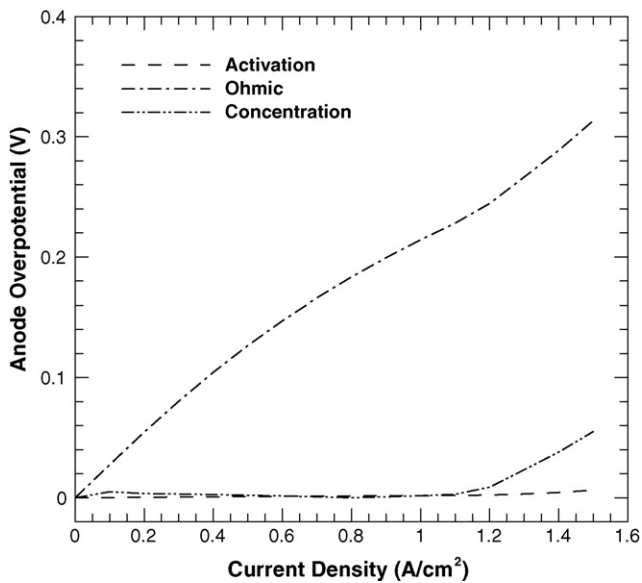
Fig. 4. The breakdown of the anode overpotentials at the base case conditions given in Table 7.

contribution of the activation overpotential is negligible. Moreover, the concentration overpotential in the thick anode remains almost constant and close to zero for most of the current density range considered in the present simulation before starting to increase beyond about 1.1 A/cm^2. The reasons for the anode concentration overpotential being negligible even in the thick anode are because of low fuel utilization (10%) and high reactant concentration due to the chemical reactions (reforming and water–gas shift reactions). For instance, methane reforming reaction produces three moles of H$_2$ for every mole of CH$_4$ consumed during the reaction; similarly, water–gas shift reaction produces a mole of H$_2$ for every mole of CO consumed during the reaction. A useful comparison of the anode concentration overpotential with and without considering these chemical reactions is shown in Fig. 5. Even at low fuel utilization, the concentration overpotential in the anode-supported SOFC becomes significant when there are no chemical reactions in the
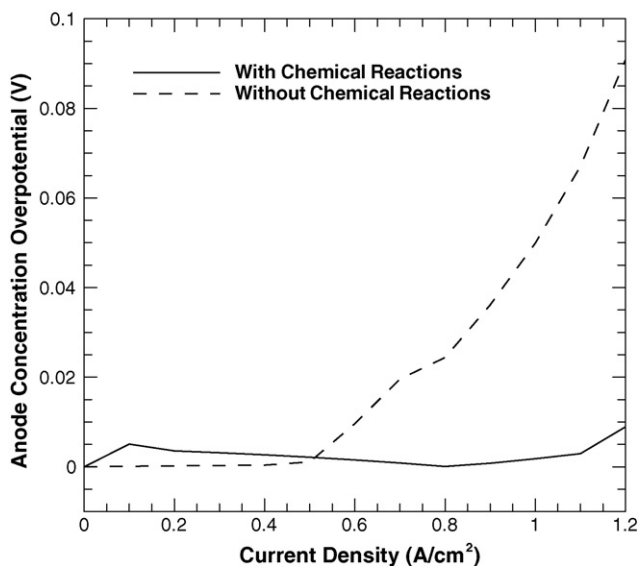
anode and can be as high as 0.1 V at higher current densities. However, it is still three orders of magnitude smaller than the anode ohmic overpotential.

In contrast to the anode concentration overpotential, the cathode concentration overpotential in an anode-supported SOFC is negligible. This is again due to the small thickness of the cathode and low oxidant utilization (10%). However, the contributions of the cathode activation and cathode ohmic overpotentials are significant to the total cell potential loss, which is evident from Fig. 6. Further, it is clear from Figs. 4 and 6 that the ohmic overpotential is the single largest contributor to the cell potential loss even in the anode-supported SOFCs, which is often reported to be negligible. Furthermore, it can be seen from Figs. 4 and 6 that the profiles of the anode and cathode ohmic overpotentials show different degrees of non-linear trends with current density. This is due to the larger thickness of the anode reaction zone layer than the cathode reaction zone layer resulting in the spatial limitation of oxide ion transport in the anode reaction zone layer [40]. Further, the temperature dependent ionic conductivity of the ion-conducting particles in the reaction zone layers contributes to the non-linear behavior of the ohmic overpotentials.

In order to probe the robustness of the model, a parametric study has been performed to examine the effect of operating and design conditions on the performance of an anode-supported SOFC. Moreover, as it is rightly stated by Alkhateeb et al. [35] that a comprehensive model would analyze the effect of macroscopic and microscopic characteristics of the electrodes on the performance of the cell. To start with, the effect of operating temperature on the performance of an anode-supported SOFC is shown in Fig. 7. Anode-supported SOFCs typically operate between 823 K and 1073 K [3]. In the present simulation, temperature in the typical range is varied to examine its effect on the performance of an anode-supported SOFC. The reaction rate constants for the chemical reactions are valid for the temperature range considered in the present simulation [20]. Further, the other operating and design parameters are kept constant in accordance with the base case parameters. It can be seen that increasing the operating temperature of the cell increases the performance of an anode-supported SOFC. It can also be seen that increasing the operating temperature increases the limiting current density, which corresponds to the current density at the zero cell potential. Moreover, the power density increases
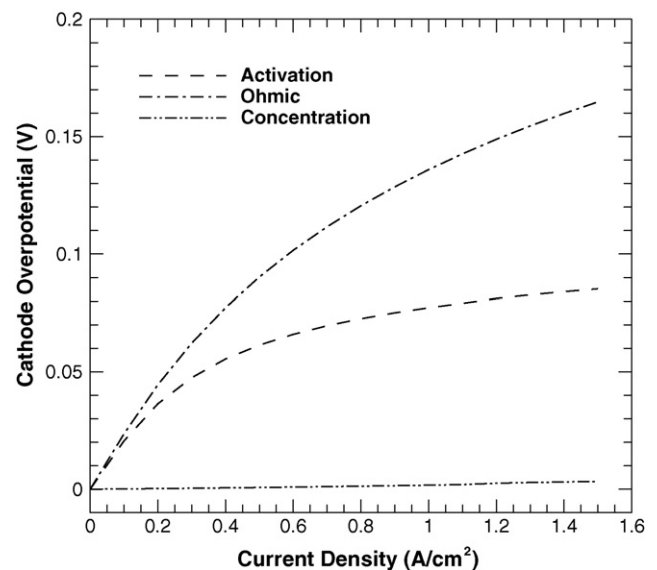

Fig. 5. Comparison of the anode concentration overpotential at the base case conditions given in Table 7. The chemical reactions refer to the methane reforming and water–gas shift reactions that produce hydrogen in the anode.

Fig. 6. The breakdown of theCathode overpotentials at the base case conditions given in Table 7.

Fig. 7. Effect of operating temperature on the performance of an anode-supported SOFC.

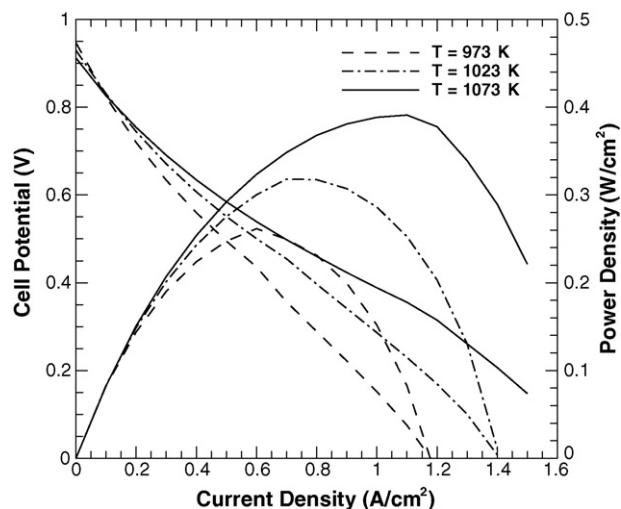**Fig. 8.** Effect of the anode reaction zone thickness on the performance of an anode-supported SOFC.

with the increase in operating temperature, with its peak shifted towards higher current densities at higher temperatures. The reason for the increase in the cell performance with temperature is primarily due to the increase in the temperature dependent ionic conductivity of the ion-conducting particles in the reaction zone layers, which in turn reduces the contribution of the ohmic overpotential of the electrodes. Further, the ionic conductivity of the electrolyte increases with the increase in operating temperature, resulting in better cell performance. The increase in the limiting current density with operating temperature is due to the fact that the molecular diffusivity of the species increases with temperature, which reduces the resistance to the mass transport in the thick anode, and thereby reduces the anode concentration overpotential with temperature. Although there are many incentives in reducing the operating temperature but there is a significant drop in cell performance just by reducing the temperature from 1073 K to 973 K, which is evident from Fig. 7. Hence, the ionic conductivity of the ion-conducting particles in the reaction zone layers and electrolyte need to be enhanced in order to operate anode-supported SOFCs below 1073 K.

The thickness of the reaction zone layers is one of the important parameters in SOFC electrodes. Different values are reported in literature, based on the thickness of the electrode ranging from 10 μm to 50 μm [11,17,36–39]. The effect of the anode reaction zone thickness on the performance of an anode-supported SOFC is shown in Fig. 8. The operating and other design parameters are kept the same as those in Table 7. In addition, the combined thickness of the anode backing layer and the reaction zone layer is kept at 2 mm. Increasing the reaction zone thickness increases TPBs in the reaction zone layer resulting in the increased rate of electrochemical reaction, which in turn reduces the activation overpotential. However, increasing the reaction zone thickness increases the distance through which oxide ions and electrons migrate to reach the reaction sites. Due to the poor ionic conductivity of the ion-conducting particles, increasing the reaction zone thickness increases the ohmic overpotential. The balance between the decrease in the activation overpotential and the increase in the ohmic overpotential reflects the improvement in the cell performance with respect to the increase in the anode reaction zone thickness. A close observation of Fig. 8 reveals that there is no significant increase in the performance when the anode reaction zone thickness is increased from 30 μm to 70 μm, in fact, the performance is reduced at higher current densities.

The effect of porosity on the performance of an anode-supported SOFC is illustrated in Fig. 9. All other operating and design param-
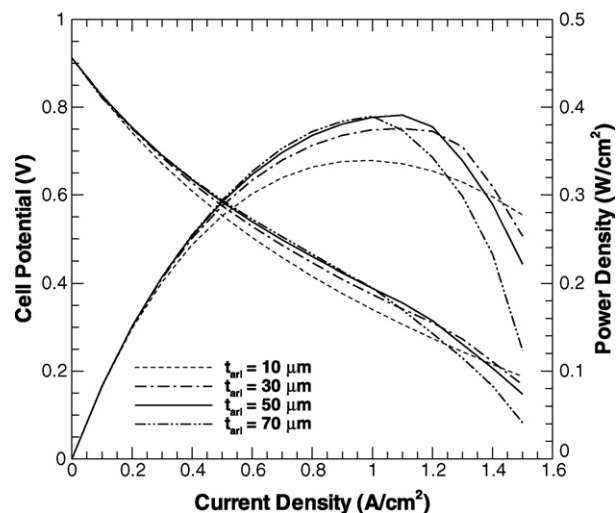
eters are kept the same as for the condition shown in Table 7. It is seen that increasing the porosity of the porous layers decreases the performance of an anode-supported SOFC; however, the performance increases with increasing the porosity at higher current densities. This is due to the reduction in mass transport resistance with increasing porosity of the porous layers at higher current densities. In contrary, increasing the porosity decreases the effective conductivities of the porous layers resulting in the increased contribution of ohmic overpotentials for most of the current density range considered in the present simulation.

Fig. 10 shows the effect of tortuosity of the porous layers on the performance of an anode-supported SOFC. Again, all the other design and operating parameters are set equal to the base case parameters given in Table 7. One of the primary deficiencies of some of the earlier models is the need to invoke unreasonably large tortuosity values in the range of 10–17 [5,41]. The reason of invoking such large tortuosities is to produce the concentration overpotential [40]. However, tortuosities for the porous layers of SOFC have been experimentally determined to be in the range of 2.5–6.0 [11,17,40,42]. Therefore, in the present simulation, tortuosity of the porous layers has been varied between 3.0 and 6.0. Increasing the tortuosity of
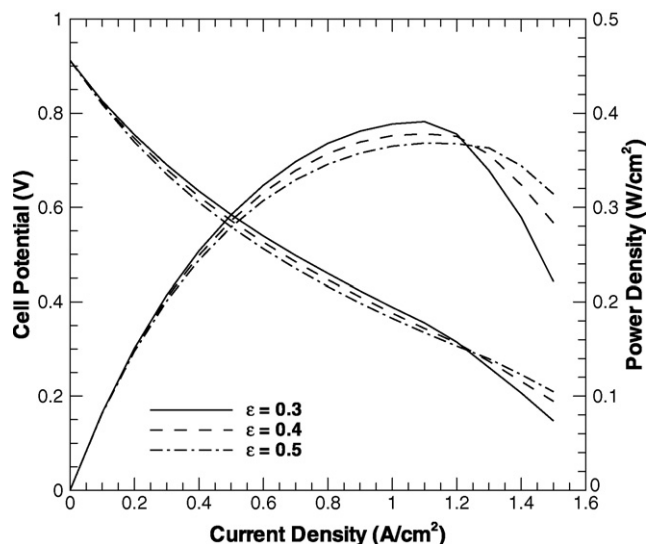

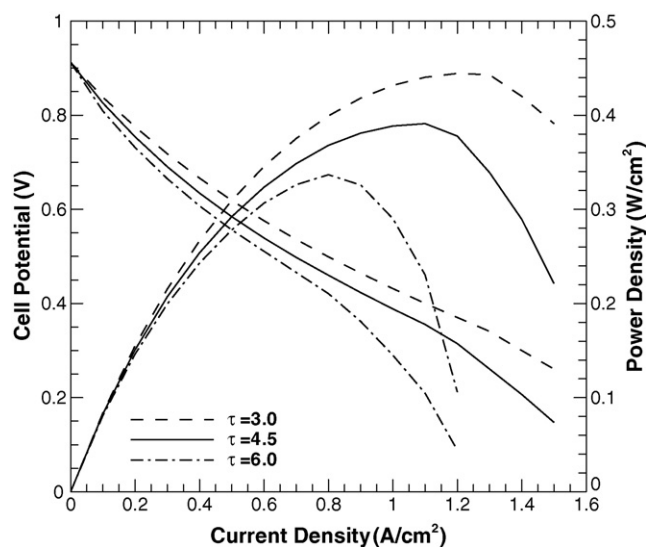**Fig. 9.** Effect of porosity on the performance of an anode-supported SOFC.

Fig. 10. Effect of tortuosity on the performance of an anode-supported SOFC.

the porous layers increases the resistance to mass diffusion due to increased diffusion path length, which results in the reduction of reactant concentration at the reaction sites; as a result, the contributions of activation and concentration overpotentials to the cell potential loss increases with the increase of tortuosity. Further, the effective conductivities of the porous layers decreases with the increase of tortuosity resulting in the increase of ohmic contribution of the porous layers to the cell potential loss, and hence cell performance decreases with the increase of tortuosity, as shown in Fig. 10.

The composition of the electron-conducting particles in the reaction zone layers is an important parameter affecting the cell performance, and its effect is shown in Fig. 11. The composition is represented by the volume fraction of the electron-conducting particles (Φ) in the reaction zone layers, which is varied from 0.4 to 0.6 and its effect on the cell performance is illustrated in Fig. 11. The other operating and design conditions remain the same as the base case parameters given in Table 7. It is seen that increasing the volume fraction of the electron-conducting particles in the reaction zone layers from 0.4 to 0.5 increases the performance of an
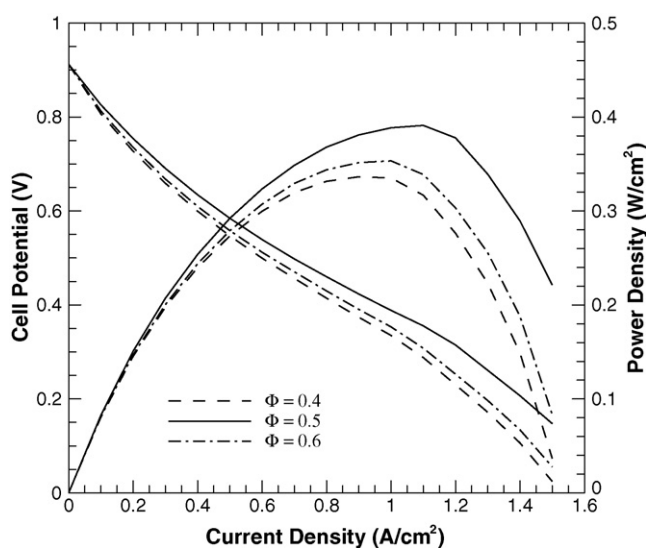
anode-supported SOFC; however, further increase in the volume fraction of the electron-conducting particles in the reaction zone layers results in the reduction of cell performance. This is due to the fact that the largest reactive surface area for electrochemical reactions is achieved when the dimensions and volume fractions of the electron- and ion-conducting particles are equal [41]. Moreover, the effective electronic and ionic conductivities in the reaction zone layers are functions of the volume fraction of the electron-conducting particles; increasing Φ beyond 0.5 increases the effective electronic conductivity but decreases the effective ionic conductivity in the reaction zone layers resulting in an increase in the ohmic overpotential, and thereby decreasing the cell performance.

6. Conclusions

A general electrode–electrolyte-assembly (EEA) model has been developed for the performance characteristics of planar anode-supported solid oxide fuel cells. One of the novel features of the present model is its treatment of the porous electrodes composed of two distinct layers, referred to as the backing layer and the reaction zone layer. The present model is fuel flexible and includes methane reforming and water–gas shift reactions in the anode. The coupled governing equations of species, charge and energy along with the constitutive equations in different layers of the cell are solved using finite volume method. The present model can predict all forms of overpotentials in the electrodes and the predicted anode concentration overpotential is validated with measured data available in literature. An excellent agreement is obtained between the predicted and measured concentration overpotential with coefficient of determination as high as 0.989. It is found that the anode overpotential is the largest contributor to the cell potential loss at higher current densities, followed by cathode and electrolyte overpotentials. Although the thicknesses of the cathode and the electrolyte in an anode-supported SOFC are negligible relative to the thickness of the anode but the contribution of cathode and electrolyte overpotentials are not negligible. In addition, even at low fuel utilizations, the contribution of anode concentration overpotential in an anode-supported SOFC becomes significant when there are no chemical reactions in the anode. However, the anode concentration overpotential is still three orders of magnitude smaller than the anode ohmic overpotential. Reducing the operating temperature below 1073 K results in a significant drop in the performance of an anode-supported SOFC; hence ionic conductivity of the ion-conducting particles in the reaction zone layers and electrolyte need to be enhanced to operate anode-supported SOFCs below 1073 K. Further, the anode reaction zone thickness of 50 μm is found to be an optimal thickness for the conditions investigated in this study.

References

[1] M.A. Khaleel, Z. Lin, P. Singh, W. Surdoval, D. Collin, Journal of Power Sources 130 (2004) 136–148.
[2] S.C. Singhal, Solid State Ionics 152–153 (2002) 405–410.
[3] P. Aguiar, C.S. Adjiman, N.P. Brandon, Journal of Power Sources 138 (2004) 120–136.
[4] H. Yakabe, M. Hishinuma, M. Uratani, Y. Matsuzaki, I. Yasuda, Journal of Power Sources 86 (2000) 423–431.
[5] J.-W. Kim, A.V. Virkar, K.-Z. Fung, K. Mehta, S.C. Singhal, Journal of the Electrochemical Society 146 (1999) 69–78.
[6] A.V. Virkar, J. Chen, C.W. Tanner, J.-W. Kim, Solid State Ionics 131 (2000) 189–198.
[7] J.H. Nam, D.H. Jeon, Electrochimica Acta 51 (2006) 3446–3460.
[8] J. Yuan, B. Sunden, Transactions of the ASME, Journal of Fuel Cell Science and Technology 3 (2006) 89–98.
[9] J. Yuan, B. Sunden, Transactions of the ASME, Journal of Heat Transfer 127 (2005) 1380–1390.
[10] T. Ackmann, L.G.J. de Haart, W. Lehnert, D. Stolten, Journal of the Electrochemical Society 150 (2003) A783–A789.
[11] W. Lehnert, J. Meusinger, F. Thom, Journal of Power Sources 87 (2000) 57–63.
[12] J. Deseure, Y. Bultel, L. Dessemond, E. Siebert, Electrochimica Acta 50 (2005) 2037–2046.

Fig. 11. Effect of the volume fraction of the electron-conducting particles in the reaction zone layers on the performance of an anode-supported SOFC.

[13] X.J. Chen, S.H. Chan, K.A. Khor, Electrochimica Acta 49 (2004) 1851–1861.
[14] S.H. Chan, Z.T. Xia, Journal of the Electrochemical Society 148 (2001) A388–A394.
[15] S. Sunde, Journal of Electroceramics 5 (2000) 153–182.
[16] P. Costamagna, P. Costa, V. Antonucci, Electrochimica Acta 43 (1998) 375–394.
[17] R.E. Williford, L.A. Chick, Surface Science 547 (2003) 421–437.
[18] J. Fleig, The Annual Review of Materials Research 33 (2003) 361–382.
[19] M.M. Hussain, X. Li, I. Dincer, International Journal of Energy Research 29 (2005) 1083–1101.
[20] B.A. Haberman, J.B. Young, International Journal of Heat and Mass Transfer 47 (2004) 3617–3629.
[21] B. Todd, J.B. Young, Journal of Power Sources 110 (2002) 186–200.
[22] T. Kenjo, S. Osawa, K. Fujikawa, Journal of the Electrochemical Society 138 (1991) 349–355.
[23] T. Kenjo, M. Nishiya, Solid State Ionics 57 (1992) 295–302.
[24] J. Abel, A.A. Kornyshev, W. Lehnert, Journal of the Electrochemical Society 144 (1997) 4253–4259.
[25] D.H. Jeon, J.H. Nam, C.-J. Kim, Journal of Power Sources 139 (2005) 21–29.
[26] J. Newman, K.E. Thomas-Alyea, Electrochemical Systems, 3rd ed., Wiley, New Jersey, 2004.
[27] R. Bove, S. Ubertini, Journal of Power Sources 159 (2006) 543–559.
[28] S.V. Patankar, Numerical Heat Transfer and Fluid Flow, McGraw-Hill, New York, 1980.
[29] H.K. Versteeg, W. Malalasekera, An Introduction to Computational Fluid Dynamics: The Finite Volume Method, John Wiley & Sons Inc., New York, 1995.
[30] N.R. Amundson, E. Morana, R. Sanders, East–West Journal of Numerical Mathematics 6 (1998) 9–25.
[31] J.M. Stockie, K. Promislow, B.R. Wetton, International Journal for Numerical Methods in Fluids 41 (2003) 577–599.
[32] H. Zhu, R.J. Kee, Journal of Power Sources 117 (2003) 61–74.
[33] S.H. Chan, C.F. Low, O.L. Ding, Journal of Power Sources 103 (2002) 188–200.
[34] J.R. Ferguson, J.M. Fiard, R. Herbin, Journal of Power Sources 58 (1996) 109–122.
[35] M.K. Alkhateeb, S.J. Parulekar, J.R. Selman, S. Al-Hallaj, Electrochemical Society Proceedings, vol. 2005–2007, 2005, pp. 738–748.
[36] N.Q. Minh, T. Takahashi, Science and Technology of Ceramic Fuel Cells, Elsevier Science B.V., Amsterdam, The Netherlands, 1995.
[37] M. Brown, S. Primdahl, M. Mogensen, Journal of the Electrochemical Society 147 (2000) 475–485.
[38] A. Bieberle, L.P. Meier, L.J. Gauckler, Journal of the Electrochemical Society 148 (2001) A646–A656.
[39] G.O. Lauvstad, R. Tunold, S. Sunde, Journal of the Electrochemical Society 149 (2002) E506–E514.
[40] R.E. Williford, L.A. Chick, G.D. Maupin, S.P. Simner, Journal of the Electrochemical Society 150 (2003) A1067–A1072.
[41] P. Costamagna, K. Honegger, Journal of the Electrochemical Society 145 (1998) 3995–4007.
[42] I. Drescher, W. Lehnert, J. Meusinger, Electrochimica Acta 43 (1998) 3059–3068.